



Seed-mediated synthesis of Pt_xAu_y@Ag electrocatalysts for the selective oxidation of glycerol

Yongfang Zhou^a, Yi Shen^{a,*}, Jingyu Xi^b

^a School of Food Science and Engineering, South China University of Technology, Guangzhou, 510640, China

^b Institute of Green Chemistry and Energy, Graduate School at Shenzhen, Tsinghua University, Shenzhen, 518055, China

ARTICLE INFO

Keywords:

Pt_xAu_y@Ag electrocatalysts
Glycerol oxidation
Selectivity
Dihydroxyacetone
C3 products

ABSTRACT

Trimetallic Pt_xAu_y@Ag nanoparticles with varying Pt/Au ratios were prepared via a seed-mediated growth process, in which Ag nanoparticles were employed as sacrificial seeds, and further evaluated as electrocatalysts for the selective oxidation of glycerol. The structures of the as-prepared Pt_xAu_y@Ag nanoparticles were characterized by transmission electron microscopy, electron energy loss spectroscopy and UV–vis absorption spectroscopy. The electrocatalytic activity of the Pt_xAu_y@Ag nanoparticles was extensively evaluated by various electrochemical methods including cyclic voltammetry, linear sweep voltammetry, and chronoamperometric measurements. The Pt_xAu_y@Ag catalysts exhibit superior activity in alkaline solutions relative to acidic solutions. In acidic solutions, the Pt₆Au₄@Ag catalyst shows the highest current density of 0.67 mA cm^{−2}, which is 2.6 times that of the Pt/C catalyst. In alkaline solutions, the Pt₄Au₆@Ag has the highest current density of 3.1 mA cm^{−2}, which is 4.7 times that of the Pt/C catalyst. The products of glycerol oxidation over the catalysts at potentials of 0.5, 0.7, 0.9, 1.1 and 1.3 V were analyzed by high performance liquid chromatography (HPLC). Nine products including oxalate acid, tartronic acid, glyoxylic acid, glyceric acid, glyceraldehyde, glycolic acid, lactic acid, dihydroxyacetone (DHA), and formic acid were detected. HPLC results show that the Pt_xAu_y@Ag catalysts tend to yield more C3 products. Notably, among the catalysts, the Pt₄Au₆@Ag yields the largest DHA selectivity of 77.1% at a potential of 1.1 V. The remarkable selectivity of the C3 products can be ascribed to the dominant Pt (111) facets in the Pt_xAu_y@Ag catalysts and the synergistic effects of Pt and Au/Ag atoms.

1. Introduction

Glycerol (GLY), a byproduct of biodiesel production, has recently attracted great attention because it could be possibly transformed into various products and intermediates via the selective oxidation such as dihydroxyacetone (DHA), glyceraldehyde (GALD), glyceric acid (GLA) and tartronic acid (TA) [1–3]. The C3 products obtained from GLY oxidation are of particular importance [4,5]. For example, DHA and GALD are widely used in the cosmetic industry as ingredients of sunless tanning lotions [6]. GLA and TA can be upgraded into various commercial products (e.g., polymers and biodegradable emulsifiers) [7]. In this context, the selective conversion of GLY into C3 products is highly desirable. Presently, the oxidation of GLY always involves strong oxidants, such as permanganate and chromic acid. The utilization of these toxic substances renders it quite difficult to control reaction pathway, giving rise to unsatisfactory selectivities towards desired products. Besides, hydrothermal oxidation of GLY has been studied to produce valuable products [8]. Unfortunately, hydrothermal processes are always

performed at high pressures and temperatures, which presents an obstacle for the large-scale application. Alternatively, GLY electro-oxidation is a totally green process, which affords a promising route to produce high value-added chemicals and intermediates. The optimization of applied potential and formulation of the catalyst offer effective strategies to tune activity and selectivity of GLY electro-oxidation [9–11].

So far, many monometallic and bimetallic catalysts have been studied for the electro-oxidation of GLY [11–19]. Pt was widely studied as a reference material for GLY oxidation in both acidic and alkaline solutions. For instance, Garcia et al. studied GLY oxidation on Pt (111) and Pt (100) electrodes [11]. They found that the products of GLY oxidation by Pt (111) electrode consisted of GALD, GLA and DHA while only GALD was obtained when the Pt (100) electrode was used. Kwon et al. studied the oxidation of GLY on polycrystalline Pt [12]. They observed that the main product of GLY oxidation was GLA in alkaline solutions while GLY was mainly converted into GALD in acidic solutions. Other low-concentration products such as DHA, TA, glycolic acid

* Corresponding author at: #381 the South China University of Technology, Wu Shan Road, Tianhe District, Guangzhou City, Guangdong Province, 510640, China.
E-mail address: feishen@scut.edu.cn (Y. Shen).

(GA), oxalic acid (OA), and formic acid (FA) were also obtained. Zhang et al. studied GLY oxidation on Pt/C catalyst in an anion-exchange membrane fuel cell [13]. They found that high solution pHs were favorable for enhancing output power density and selectivities of C3 acids.

Au is inactive in acidic solutions, but capable of catalyzing GLY oxidation in alkaline solutions [12]. Qi et al. reported a mechanistic study on GLY oxidation by Au/C catalysts [15]. The results suggested that the oxidation of the two primary OH groups of GLY was favorable while further oxidation of the secondary OH group and the cleavage of C–C bonds were greatly suppressed. Ag itself has no activity toward GLY oxidation in both acidic and alkaline solutions [16]. However, the introduction of Ag into Pt and Au crystals greatly enhances the activity and/or selectivity. Garcia et al. synthesized a MnO_x/C supported PtAg catalyst which facilitated the breakage of the C–C bonds, promoting the formation of C1 products [17]. Thia et al. studied GLY oxidation on a porous AuAg catalyst, which showed excellent activity and selectivities of FA and GA [18]. Bimetallic PtAu catalysts were also studied for GLY oxidation. Dai et al. studied GLY oxidation by PtAu catalysts and reported a lactic acid (LA) selectivity of 73% from an Au-enriched PtAu catalyst [19].

As discussed above, Pt, Au and Ag show distinct electrochemical features towards GLY oxidation. The combination of these elements could result in enhanced activity and selectivity. A thorough literature survey reveals that many monometallic and bimetallic catalysts have been reported for GLY oxidation while few studies have focused on trimetallic catalysts [9,20]. Herein, a series of $\text{Pt}_x\text{Au}_y\text{@Ag}$ nanoparticles (NPs) with a core-shell structure were synthesized and further examined as electrocatalysts for GLY oxidation. The catalytic activity and the products of GLY oxidation over the catalysts were investigated in detail. To the best of the authors' knowledge, there has been no attempt to explore the activity and products of GLY oxidation over trimetallic PtAuAg NPs so far.

2. Experimental section

2.1. Chemicals

GLY ($\geq 99\%$) was purchased from the Sinopharm Chemical Reagent Co. Ltd., China. L-(+)- GALD ($\geq 90\%$), DHA ($\geq 99\%$), D-GLA sodium salt ($\geq 95\%$), TA ($\geq 97\%$), GA ($\geq 99\%$), FA ($\geq 98\%$), OA ($\geq 99.8\%$), LA ($\geq 98\%$), and GLOA ($\geq 98\%$), AgNO_3 ($\geq 99\%$), H_2PtCl_6 solution (8 wt. %), HAuCl_4 solution (8 wt. %) were obtained from the Sigma-Aldrich, China. A commercial Pt/C catalyst (40 wt.%) was purchased from the E-TEK company.

2.2. Synthesis of $\text{Pt}_x\text{Au}_y\text{@Ag}$ NPs

Ag seeds were prepared via a reported hydrothermal process [21]. To control the size distribution of the Ag seeds, a centrifuge-selection process was conducted. The details of the size-sieving process are listed as follows: the Ag colloids were first centrifuged at a speed of 6000 rpm for 8 min to remove the large particles. The yellowish supernatant was further centrifuged at a speed of 10,000 rpm for 10 min and the resulting precipitate was employed as seeds. $\text{Pt}_x\text{Au}_y\text{@Ag}$ NPs were prepared via a seed-mediated growth approach, where Ag seeds were employed as sacrificial templates [22,23]. First, 100 mg of polyvinyl pyrrolidone (PVP) and 500 mg of citric acid were dissolved in 24 mL of deionized water, followed by stepwise addition of 15 mL of the resulting Ag seeds. The mixture was pre-heated at 90°C for at least 10 min. Next, predetermined volumes of 10 mM H_2PtCl_6 and 10 mM HAuCl_4 were added drop by drop to the suspension. The reaction was carried out at 90°C for 3 h. Subsequently, the sample was collected and washed by saturated NaCl solution for several times. Finally, the product was washed and dispersed in distilled water for further use. Six samples with Pt/Au ratios of 7:3, 6:4, 5:5, 4:6, 3:7 and 2:8 were

prepared and the resulting samples are denoted as $\text{Pt}_7\text{Au}_3\text{@Ag}$, $\text{Pt}_6\text{Au}_4\text{@Ag}$, $\text{Pt}_5\text{Au}_5\text{@Ag}$, $\text{Pt}_4\text{Au}_6\text{@Ag}$, $\text{Pt}_3\text{Au}_7\text{@Ag}$, and $\text{Pt}_2\text{Au}_8\text{@Ag}$, respectively. For comparison, Au NPs were synthesized according to the method reported by Chen et al. [24].

2.3. Structural characterization

A transmission electron microscopy (TEM, JEOL JEM-2010) was used to examine the morphology of the catalysts. An electron energy loss spectroscopy (EELS) equipped in the TEM was employed to analyze the composition of the catalysts. The optical absorption spectra of the samples were recorded using a UV-vis spectrometer (Rayleigh UV-1801).

2.4. Electrochemical measurements

Electrochemical measurements were conducted using a potentiostat (CHI 660E) connecting with a conventional three-electrode cell. A glassy carbon electrode with a diameter of 3 mm was used as a working electrode which was mechanically polished to a mirror-like finish with alumina powder (0.05 μm). The catalyst powder was transferred into the electrode via a coating process. The details of the experimental procedures can be found from the authors' previous work [25–28]. The loading of the catalyst in the electrode is ca. $500 \mu\text{g cm}^{-2}$. An Hg/HgO electrode and a Pt gauze (geometric area: $1 \times 1 \text{ cm}^2$) were utilized as reference and counter electrodes, respectively.

For product analysis, the oxidation of GLY was carried out using an H-type cell as described in the authors' previous work [27,28]. A graphite paper with dimension of $10 \times 10 \text{ mm}$ was utilized as a working electrode. Chronoamperometric (CA) tests were done at five potentials, i.e., 0.5, 0.7, 0.9, 1.1 and 1.3 V in a solution of 0.5 M KOH and 0.5 M GLY. After CA tests, the electrolyte solution was collected with a syringe for high performance liquid chromatography (HPLC) analysis.

Prior to the experiments, dissolved oxygen was removed by bubbling high-purity N_2 gas through the solution for at least 30 min. All the electrochemical measurements were conducted at room temperature ($25 \pm 1^\circ\text{C}$). The current densities reported in this work were normalized by the electrochemical active surface areas of platinum. For a good comparison, the potentials reported in this work were referenced to reversible hydrogen electrode (RHE).

2.5. Product analysis

The products of GLY oxidation were analyzed using an HPLC (Agilent 1260 Infinity II, Agilent Technologies) equipped with an Aminex HPX-87H (Bio-Rad) column. The products were detected with a refractive index detector (RID) and a diode array detector (DAD). The eluent was 5 mM H_2SO_4 with a flow rate of 0.5 mL min^{-1} and the temperature of the column was kept at 65°C . The details of the experimental procedures were reported in the authors' previous work [14,28]. The selectivity (S_i) of product was calculated using following equation: $S_i = c_i / \sum c_i$, where c_i is the concentration of product i .

3. Results and discussion

3.1. Structural properties

$\text{Pt}_x\text{Au}_y\text{@Ag}$ NPs were synthesized via a seed-mediated growth process, where Ag seeds with sizes of 20–30 nm (see Fig. S1) were employed as sacrificial templates. Fig. 1 shows the representative TEM images of the $\text{Pt}_5\text{Au}_5\text{@Ag}$ NPs. The sizes of the $\text{Pt}_5\text{Au}_5\text{@Ag}$ NPs increase to ca. 40–50 nm because of the deposition of Pt and Au [29]. The surface of the $\text{Pt}_5\text{Au}_5\text{@Ag}$ NPs is rather rough, indicating that the deposition of Pt and Au is not uniform. A large number of granular protuberances are noted from the NPs. Fig. 1c–e show the magnified view of the spots marked with A, B and C in Fig. 1b, respectively. HR-TEM

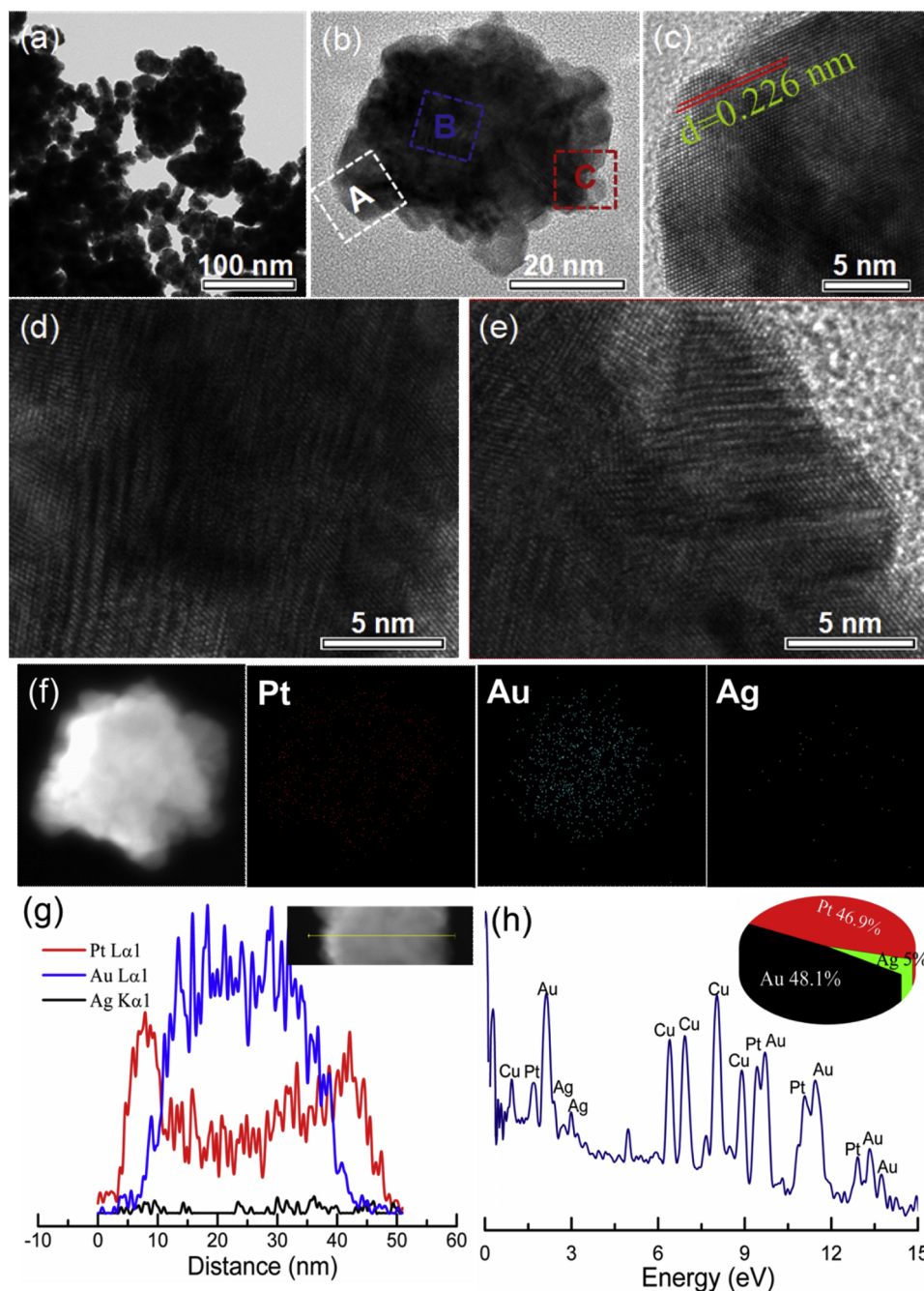
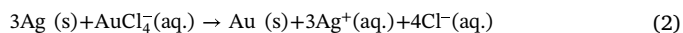
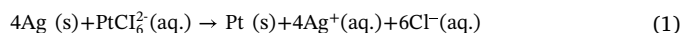


Fig. 1. (a, b) representative TEM images, (c–e) HR-TEM images, (f) HAADF-STEM image and EELS elemental mapping micrographs (g) line scan profile, and (h) EDX spectrum of Pt₅Au₅@Ag NPs.

image shown in Fig. 1c displays the continuous and well-resolved fringes with a spacing value of 0.226 nm, which is well matched with the interplanar distance of the (111) facets of face-centered cubic Pt crystals [30]. Fig. 1d and e show clear distorted lattice fringes, indicating strong strain in the NP. Lattice strain directly correlates to the location of the d-band center of the crystals [31], which could greatly affect the activity the NPs. Fig. 1f shows the high-angle annular dark-field scanning TEM (HAADF-STEM) image. It shows a distinct contrast between the core and shell of the NP, which is consistent with the TEM image shown in Fig. 1b. The corresponding EELS mapping images indicate the existence of Au, Ag and Pt elements in the NP. Fig. 1g shows the line scanning profile of the elements. Strong signals of Pt and Au are noted from the profile. In contrast, the signal of Ag is quite weak, indicating that the Ag seeds are almost completely etched [32]. It can be

seen that the signal of Au is stronger in the center of the NP while that of Pt is stronger at the edge of the NP, manifesting the formation of a well-defined core-shell structure. Further inspection on the profiles could reveal that the thickness of the Pt-enriched shell is ca. 5 nm while that of Au-enriched core is ca. 30 nm. The formation of those core-shell NPs could be related to the galvanic replacement reaction as shown in Eqs. (1) and (2) [33,34]. The elemental analysis result shown in Fig. 1h further confirms that the Pt₅Au₅@Ag NPs mainly consist of Pt (46.9%) and Au (48.1%). The content of Ag (5%) is quite limited.



Moreover, to further reveal the structure of the Pt_xAu_y@Ag, UV–vis spectroscopy has been used. Fig. S2 shows the UV–vis spectra of the

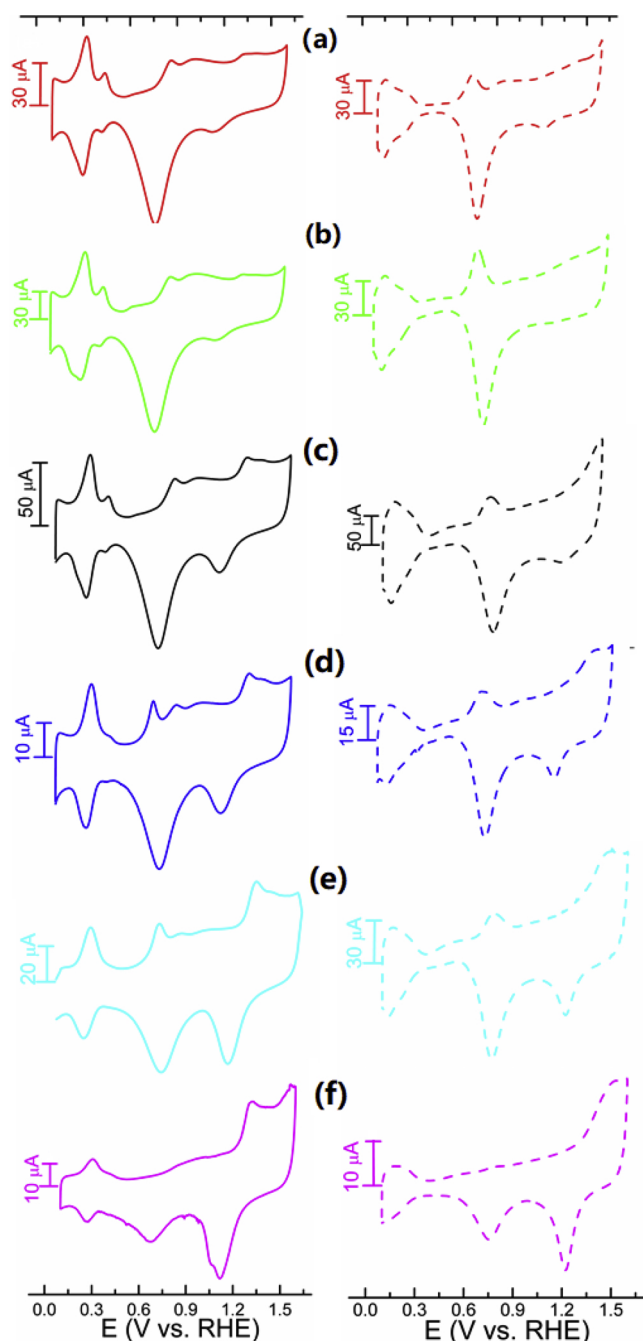


Fig. 2. CVs of (a) $\text{Pt}_7\text{Au}_3@\text{Ag}$ (b) $\text{Pt}_6\text{Au}_4@\text{Ag}$ (c) $\text{Pt}_5\text{Au}_5@\text{Ag}$ (d) $\text{Pt}_4\text{Au}_6@\text{Ag}$ (e) $\text{Pt}_3\text{Au}_7@\text{Ag}$, and (f) $\text{Pt}_2\text{Au}_8@\text{Ag}$ catalysts, recorded at 50 mV s^{-1} in 1 M KOH (solid lines) and 1 M HClO_4 (dotted lines) respectively.

samples. Curves 1 and 9 are the UV–vis spectra of the Ag and Au NPs, respectively. Strong absorption peak located at 420 and 560 nm are noted from the Ag and Au NPs, respectively, due to the excitation of surface plasmon resonance in the crystals. The spectrum of the Pt NPs (Curve 7) shows no distinct absorption in the UV–vis region, which is consistent with the properties of Pt NPs [35]. With the addition of Pt, the absorption of the $\text{Pt}_x\text{Au}_y@\text{Ag}$ NPs decreases, indicating that the Au/Ag is covered by Pt atoms, which is consistent with the TEM results. The UV–vis results confirm the formation of trimetallic $\text{Pt}_x\text{Au}_y@\text{Ag}$ NPs with a core-shell structure instead of mixture of Pt, Au and Ag NPs.

3.2. Electrochemical characterization of the catalysts

The electrochemical characterization of the $\text{Pt}_x\text{Au}_y@\text{Ag}$ NPs was implemented by cyclic voltammogram (CV) measurements conducted in both alkaline and acidic solutions as shown in Fig. 2. All the CV curves are characteristic of three processes including hydrogen adsorption-desorption, Pt surface oxidation-reduction and Au surface oxidation-reduction. Based on the CV curves, the Pt/Au ratios of the $\text{Pt}_7\text{Au}_3@\text{Ag}$, $\text{Pt}_6\text{Au}_4@\text{Ag}$, $\text{Pt}_5\text{Au}_5@\text{Ag}$, $\text{Pt}_4\text{Au}_6@\text{Ag}$, $\text{Pt}_3\text{Au}_7@\text{Ag}$, and $\text{Pt}_2\text{Au}_8@\text{Ag}$ surface were determined to be 2.15, 1.53, 1.21, 0.62, 0.45 and 0.24, respectively. Notably, compared with the CV curves of the polycrystalline Pt (See Fig. S3 and S4), those of the $\text{Pt}_x\text{Au}_y@\text{Ag}$ show a well-defined peak located at $0.7 \sim 0.8 \text{ V}$ in the forward scan, corresponding to the oxidation of Pt (111) domains [36]. Such a prominent feature is indicative of abundant Pt (111) facets in the Pt shell, which is consistent with the TEM result. In alkaline solutions, the peaks related to hydrogen desorption are present at $0.2 \sim 0.5 \text{ V}$ in the forward scan while the oxidation of Pt surface occurs at $0.75 \sim 1.1 \text{ V}$. The peaks associated with the oxidation and reduction of Au are located at 1.35 and 1.15 V, respectively, which overlap with those of Ag (see Fig. S3 and S4) [18]. In acidic solutions, the peaks related to hydrogen adsorption-desorption are less defined compared with those in alkaline solutions. In contrast, the peak associated with the oxidation of Pt (111) facets is more pronounced. The potential of this peak is very close to that of the reduction peak, suggesting that the oxidation-reduction of Pt (111) facets is highly reversible. Compared with the Au NPs, the $\text{Pt}_x\text{Au}_y@\text{Ag}$ NPs show suppressed redox peaks of Au, indicating that some of Au atoms are covered by Pt atoms. With increasing Au content, the peaks related to the redox of $\text{Au}^0/\text{Au}^{\text{I}}$ become prominent while those related to hydrogen desorption-adsorption and Pt oxidation-reduction are weakened. In particular, the peak related to the oxidation of Pt (111) facets disappears from the CV curve of the $\text{Pt}_2\text{Au}_8@\text{Ag}$ NPs, which could be probably due to the enrichment of Au atoms in the shell [37,38]. It is demonstrated that the CV curves of the $\text{Pt}_x\text{Au}_y@\text{Ag}$ NPs show distinct features compared with those of the single Pt, Au and Ag NPs owing to the unique structure and synergistic effects of the components.

3.3. Electrochemical activity

The activity of the as-synthesized $\text{Pt}_x\text{Au}_y@\text{Ag}$ NPs toward GLY oxidation in alkaline (0.1 M KOH + 1 M GLY) and acidic (0.1 M HClO_4 + 1 M GLY) solutions was examined by linear sweep voltammetry (LSV). For comparison, the activity of a commercial Pt/C catalyst was measured. The LSV results are summarized in Table S1. The $\text{Pt}_x\text{Au}_y@\text{Ag}$ NPs exhibit better reaction kinetics at low potentials as illustrated by the negative shifts in the onset potentials when compared with the Pt/C. In acidic solutions, the onset potentials of the $\text{Pt}_7\text{Au}_3@\text{Ag}$, $\text{Pt}_6\text{Au}_4@\text{Ag}$, $\text{Pt}_5\text{Au}_5@\text{Ag}$, $\text{Pt}_4\text{Au}_6@\text{Ag}$, $\text{Pt}_3\text{Au}_7@\text{Ag}$, and $\text{Pt}_2\text{Au}_8@\text{Ag}$ NPs are 0.48, 0.52, 0.49, 0.50, 0.54, and 0.43 V, respectively, which are smaller than that of the Pt/C (0.61 V) as shown in Fig. 3. The peak current densities of the $\text{Pt}_7\text{Au}_3@\text{Ag}$ (0.27 mA cm^{-2}), $\text{Pt}_6\text{Au}_4@\text{Ag}$ (0.25 mA cm^{-2}) and $\text{Pt}_5\text{Au}_5@\text{Ag}$ (0.27 mA cm^{-2}) are larger than that of the Pt/C (0.19 mA cm^{-2}) while those of the $\text{Pt}_4\text{Au}_6@\text{Ag}$ (0.15 mA cm^{-2}), $\text{Pt}_3\text{Au}_7@\text{Ag}$ (0.03 mA cm^{-2}) and $\text{Pt}_2\text{Au}_8@\text{Ag}$ (0.01 mA cm^{-2}) are smaller than that of the Pt/C. Fig. 4 shows the LSV curves recorded in alkaline solutions. The onset potentials of the $\text{Pt}_7\text{Au}_3@\text{Ag}$, $\text{Pt}_6\text{Au}_4@\text{Ag}$, $\text{Pt}_5\text{Au}_5@\text{Ag}$, $\text{Pt}_4\text{Au}_6@\text{Ag}$, $\text{Pt}_3\text{Au}_7@\text{Ag}$, and $\text{Pt}_2\text{Au}_8@\text{Ag}$ are 0.49, 0.61, 0.49, 0.58, 0.51, and 0.53 V, corresponding to peak current densities of 0.68, 1.51, 1.55, 2.50, 2.35 and 1.49 mA cm^{-2} , respectively, which are larger than that of the Pt/C (0.64 mA cm^{-2}). The LSV curves recorded in acidic solutions are smoother than those in alkaline solutions. This can be ascribed to the fact that Au is active for GLY oxidation in alkaline solutions but

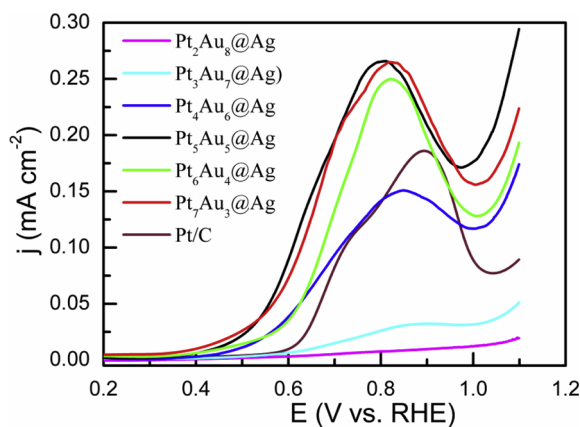


Fig. 3. LSV curves of GLY oxidation recorded with a scan rate of 10 mV s^{-1} in a solution of 0.1 M HClO_4 and 1 M GLY .

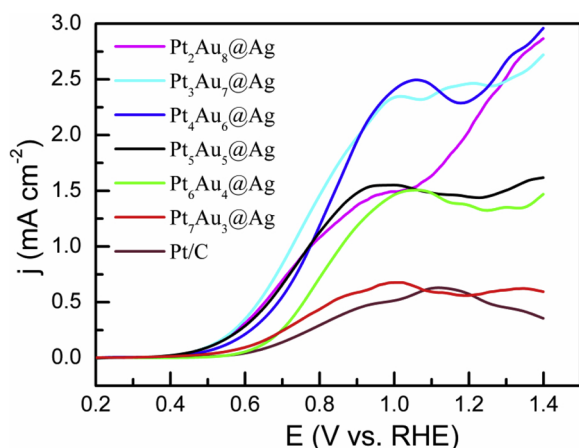


Fig. 4. LSV curves of GLY oxidation recorded with a scan rate of 10 mV s^{-1} in a solution of 0.1 M KOH and 1 M GLY .

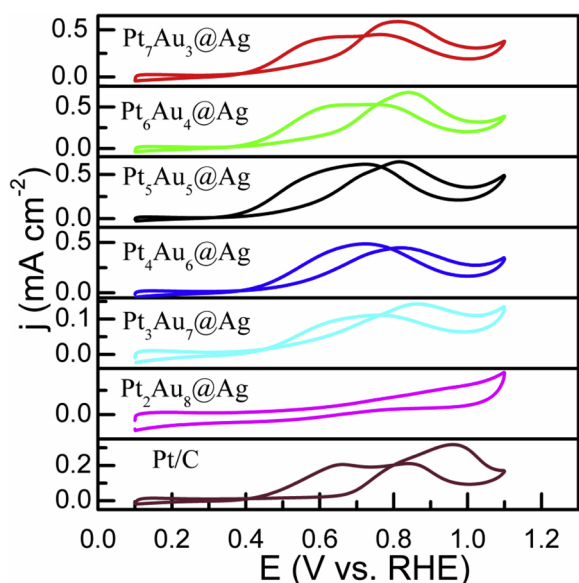


Fig. 5. CV curves of GLY oxidation recorded with a scan rate of 50 mV s^{-1} in a solution of 0.1 M HClO_4 and 1 M GLY .

shows no activity in acidic solutions as shown in Fig. S5 and S6 [12].

The activity of the $\text{Pt}_x\text{Au}_y\text{@Ag}$ NPs was further examined by CVs in acidic and alkaline solutions as shown in Figs. 5 and 6. The

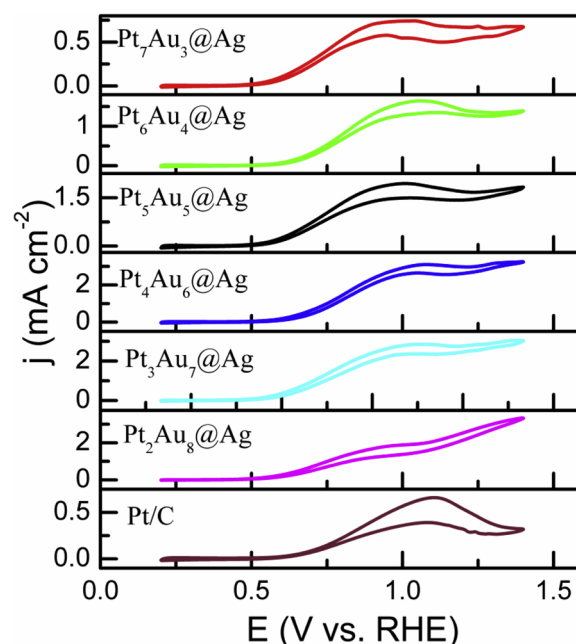


Fig. 6. CV curves of GLY oxidation recorded with a scan rate of 50 mV s^{-1} in a solution of 0.1 M KOH and 1 M GLY .

corresponding results are listed in Table S2. In acidic solutions, the current density follows the sequence of $\text{Pt}_6\text{Au}_4\text{@Ag} > \text{Pt}_5\text{Au}_5\text{@Ag} > \text{Pt}_7\text{Au}_3\text{@Ag} > \text{Pt}_4\text{Au}_6\text{@Ag} > \text{Pt/C} > \text{Pt}_3\text{Au}_7\text{@Ag} > \text{Pt}_2\text{Au}_8\text{@Ag}$, manifesting that the Pt/Au ratio affects the activity of the catalyst. An appropriate amount of Au in the catalysts could promote GLY oxidation based on the so-called bi-functional and electronic effects [38]. However, an excess of Au will reduce the active sites owing to its inactivity toward GLY oxidation in acidic solutions, thus leading to lower activity. In alkaline solutions, the $\text{Pt}_7\text{Au}_3\text{@Ag}$, $\text{Pt}_6\text{Au}_4\text{@Ag}$, $\text{Pt}_5\text{Au}_5\text{@Ag}$, $\text{Pt}_4\text{Au}_6\text{@Ag}$, $\text{Pt}_3\text{Au}_7\text{@Ag}$ and $\text{Pt}_2\text{Au}_8\text{@Ag}$ have forward current densities of 0.74, 1.64, 1.94, 3.10, 2.85, 1.86 mA cm^{-2} , which are 1.1, 2.5, 2.9, 4.7, 4.3, and 2.8 times that of the Pt/C, respectively. Notably, the peak current densities in acidic solutions are much lower than those in alkaline solutions, which is due to the sluggish kinetics in acidic solutions [12]. For better comparison, CVs of the Pt/C, Au and Ag were also recorded as shown in Fig. S7 and S8. It confirms that Ag is not active for GLY oxidation in both acidic and alkaline solutions, and that Au is active only in alkaline solutions.

The performance of the catalysts was characterized by CA tests. The CA tests were carried out under applied potentials of 1.3, 1.1, 0.9, 0.7, and 0.5 V. The selection of these five potentials was based on the CV curves shown in Fig. 6. As shown in Fig. S9, the current density dramatically decreases in the initial several seconds due to the capacitive current decay and then gradually reaches to a constant stage [39]. It can be seen that the current densities of the $\text{Pt}_4\text{Au}_6\text{@Ag}$ and $\text{Pt}_3\text{Au}_7\text{@Ag}$ are higher than those of other catalysts at the five potentials, which is consistent with the LSV and CV results. The electrochemical results suggest that the $\text{Pt}_x\text{Au}_y\text{@Ag}$ catalysts possess better activity than the Pt/C and Au catalysts in alkaline solutions. In particular, among the catalysts, the $\text{Pt}_6\text{Au}_4\text{@Ag}$ catalyst shows the best activity in acidic solutions while the $\text{Pt}_4\text{Au}_6\text{@Ag}$ catalyst exhibits superior activity in alkaline solutions.

3.4. Product analysis and reaction pathway

For product analysis, the electrolyte solution was analyzed by HPLC. The concentration of the product was determined based on the calibrated curves as shown in Fig. S10. Fig. S11a and b show the representative HPLC curves obtained from DAD ($\lambda = 220, 210$, and

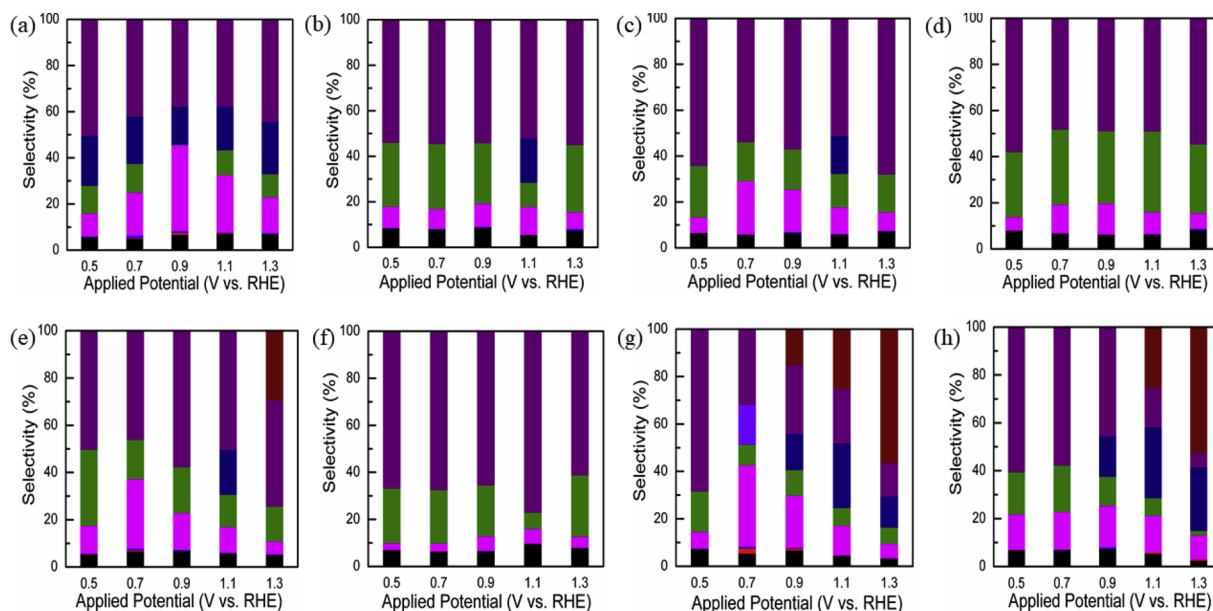


Fig. 7. Product distributions under different applied potentials over the (a) Pt, (b) Au, (c) Pt₇Au₃@Ag, (d) Pt₆Au₄@Ag, (e) Pt₅Au₅@Ag, (f) Pt₄Au₆@Ag, (g) Pt₃Au₇@Ag, and (h) Pt₂Au₈@Ag catalysts in a solution of 0.5 M GLY and 0.5 M KOH. Black: OA; Red: TA; Blue: GLOA; Magenta: GLA; Olive: GALD; Navy: GA; Violet: LA; Purple: DHA; and Wine: FA (For interpretation of the references to colour in this figure legend, the reader is referred to the web version of this article).

194 nm) and RID detectors, respectively. Notably, some of the products are present as salts in alkaline solutions but denoted as acid forms in this work for simplicity.

Fig. 7 shows the product distribution at different applied potentials. The concentrations of the products are summarized in Table S3-7. When the Pt/C is used, the products of GLY oxidation consist of considerable DHA, GA, GLA, GALD and OA, and a trace of GLOA and TA while no LA and FA are detected as shown in Fig. 7a. The selectivity of DHA is highest at the five potentials. GLA selectivity increases with increasing applied potential from 0.5 to 0.9 V and then decreases thereafter, leading to a maximum selectivity of 37.4% at 0.9 V. Such a trend is contrary with GA selectivity. When the Au is used as a catalyst, abundant DHA, GALD, GLA and OA, a trace of GLOA, but no TA, LA and FA are obtained as shown in Fig. 7b. Interestingly, GA is only detected at 1.1 V. The product distribution of the Pt₇Au₃@Ag is shown in Fig. 7c. DHA is also the major product and a maximum value of 67.8% is obtained at 1.3 V. Similar to the Au catalyst, GA is only detected at 1.1 V. GLA selectivity initially increases from 6.7% at 0.5 V to 23.3% at 0.7 V and then decreases with further increasing potential. The GALD selectivity of the Pt₇Au₃@Ag is higher than that of the Pt/C, but lower than that of the Au. Compared with the Pt/C, the Pt₆Au₄@Ag yields more GALD, but less GLA as shown in Fig. 7d. Notably, no GA is produced at the five potentials. DHA selectivity is similar to that of the Pt₇Au₃@Ag, giving the largest value of 57.9% at 0.5 V. The Pt₅Au₅@Ag also shows the higher GALD selectivity compared with the Pt/C as shown in Fig. 7e. GLA selectivity increases from 11.9% at 0.5 V to 29.5% at 0.7 V, and then decreases thereafter. Such a trend is also noted from the Pt₇Au₃@Ag. Similar to the Au and Pt₇Au₃@Ag, GA can only be detected at 1.1 V. It is noteworthy that a FA selectivity of 29.2% is obtained at 1.3 V. Compared with the Pt/C, the Pt₄Au₆@Ag yields more DHA, but less GLA as shown in Fig. 7f. Notably, among the catalysts, the Pt₄Au₆@Ag yields the largest DHA selectivity. In particular, a remarkable DHA selectivity of 77.1% is obtained at 1.1 V. GA and FA are not detected at the applied potentials. GALD distribution of the Pt₄Au₆@Ag is similar to that of the Au, showing the lowest selectivity of 6.9% at 1.1 V. When the Pt₃Au₇@Ag is used, GLA selectivity increases from 7.1% at 0.5 V to 34.5% at 0.7 V and then decreases thereafter while DHA selectivity decreases with increasing applied potential as shown in Fig. 7g. Notably, both GA and FA are detected at high

potentials. GA selectivities of 15.2, 27.3 and 13.1% and FA selectivities of 15.2, 25.0 and 56.3% are obtained at the potentials of 0.9, 1.1 and 1.3 V, respectively. More interestingly, the Pt₃Au₇@Ag is the only one which could produce LA from GLY. When the Pt₂Au₈@Ag is used, similar to the Pt₃Au₇@Ag, DHA selectivity decreases sharply with increasing potentials, leading to a minimum selectivity of 6.1% at 1.3 V as shown in Fig. 7h. The Pt₂Au₈@Ag shows GLA selectivities of 14.8, 15.7, 17.4, 15.3, and 10.1% at the potentials of 0.5, 0.7, 0.9, 1.1, and 1.3 V, which are 1.6, 1.8, 1.7, 1.3, 1.4 times those of the Au, respectively. The Pt₂Au₈@Ag yields considerable FA and GA, but negligible GALD at high potentials.

For clarity, the selectivity of the product is plotted against the catalyst as shown in Fig. S12-20. Considerable DHA is produced from all the catalysts at the five applied potentials as shown in Fig. S12. The applied potential has limited effects in the DHA selectivities of the Pt/C, Pt₇Au₃@Ag, Pt₆Au₄@Ag, Pt₅Au₅@Ag, Pt₄Au₆@Ag and Au catalysts while those of the Pt₃Au₇@Ag and Pt₂Au₈@Ag catalysts decrease with increasing potential. The GALD selectivity of the Pt₆Au₄@Ag is larger than other catalysts at the potentials of 0.7, 0.9, 1.1, and 1.3 V, giving the largest value of 35% at 1.1 V as shown in Fig. S13. No GALD is obtained from the Pt/C at 0.9 V. GLA selectivities of the catalysts are highly dependent on the applied potential. The Pt₃Au₇@Ag possesses the largest GLA selectivity of 34.5% at 0.7 V as shown in Fig. S14. Among the catalysts, the Pt₄Au₆@Ag produces least GLA at the applied potentials. The Pt/C, Pt₆Au₄@Ag and Pt₂Au₈@Ag yield the largest GLA selectivity at 0.9 V while the Pt₇Au₃@Ag, Pt₅Au₅@Ag and Pt₃Au₇@Ag exhibit the largest GLA selectivity at 0.7 V. GA is prone to being generated at high potentials. The largest GA selectivity of 29.5% is obtained from the Pt₂Au₈@Ag at 1.1 V as shown in Fig. S15. Notably, the Pt₆Au₄@Ag and Pt₄Au₆@Ag yield no GA at the five potentials. GA can only be obtained from the Pt₇Au₃@Ag and Pt₅Au₅@Ag at 1.1 V. In contrast, GA can be obtained from the Pt/C at all the applied potentials. FA is detected from the Pt₅Au₅@Ag, Pt₃Au₇@Ag and Pt₂Au₈@Ag as shown in Fig. S16. FA selectivities of the Pt₃Au₇@Ag and Pt₂Au₈@Ag increase with increasing potential. The largest FA selectivity of 56.3% is obtained from the Pt₃Au₇@Ag at 1.3 V. LA can only be obtained from the Pt₃Au₇@Ag at 0.7 V as shown in Fig. S17. OA is produced by all the catalysts, but its selectivity is not more than 10% as shown in Fig. S18. For all the catalysts, TA and GLOA selectivities are less than 2.5% as

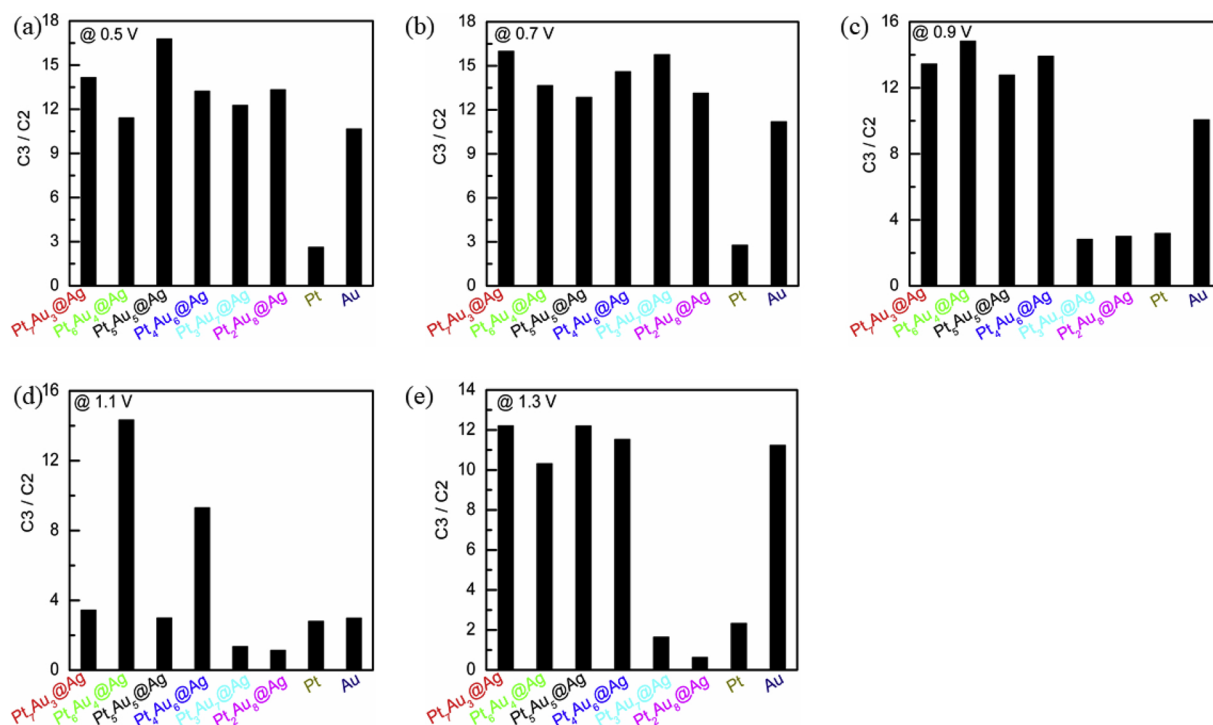


Fig. 8. C3/C2 ratios of the catalysts at applied potentials of (a) 0.5, (b) 0.7, (c) 0.9, (d) 1.1, and (e) 1.3 V.

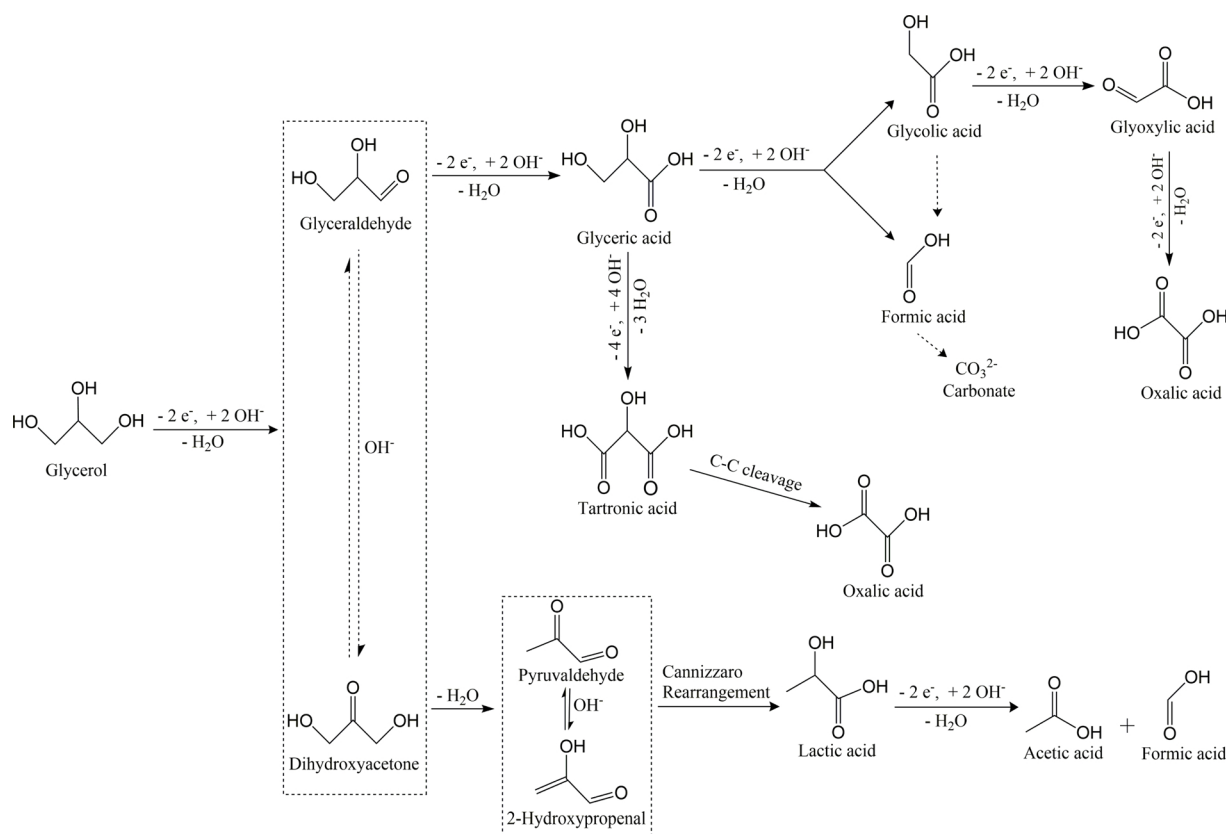
shown in Fig. S19 and S20.

Since the C3 products obtained from GLY oxidation are of particular importance, the resulting products in this work are categorized into C3 (DHA, GALD, GLA, LA and TA) and C2 products (GA, OA and GLOA). Fig. 8 shows the C3/C2 ratios of the catalysts. It clearly shows that the Pt_xAu_y@Ag catalysts possess larger C3/C2 ratios at 0.5 and 0.7 V, compared with the Pt/C and Au catalysts. The highest C3/C2 ratio of 16.8 is obtained from the Pt₅Au₅@Ag at 0.5 V, indicating that the Pt₅Au₅@Ag tends to generate more C3 products. At the potentials of 0.9, 1.1 and 1.3 V, the C3/C2 ratios of the Pt₃Au₇@Ag and Pt₂Au₈@Ag are lower than those of the Pt/C and Au catalysts. The Pt₇Au₃@Ag shows the C3/C2 ratios of 14.2, 16, 13.4, 3.4, and 12.2 at the applied potentials of 0.5, 0.7, 0.9, 1.1, and 1.3 V, which is 5.5, 5.7, 4.2, 1.2, and 5.3 times those of the Pt/C, respectively. The Pt₆Au₄@Ag and Pt₄Au₆@Ag exhibit the larger C3/C2 ratios than the Pt/C and Au catalysts at all the applied potentials. In particular, at 0.9 V, the Pt₆Au₄@Ag shows a large C3/C2 ratio of 14.8, which is 4.6 and 1.5 times that of the Pt/C and Au catalysts, respectively.

On the basis of the HPLC results, the pathways of GLY oxidation by the Pt_xAu_y@Ag are proposed as illustrated in Scheme 1. GLY is first oxidized to GALD or DHA by deprotonating two-electrons. The resulting DHA and GALD is a pair of isomers and present in an equilibrium state in alkaline solutions [40]. Compared with the Pt/C and Au, the Pt_xAu_y@Ag catalysts exhibit the higher DHA concentrations at low potentials, indicating that the Pt_xAu_y@Ag catalysts facilitate to generate more DHA at low potentials, which is attributed to the facile removal of intermediates of GLY oxidation arisen from the bi-functional effects, strain effects and dominant Pt (111) facets in the catalysts. GALD tends to be produced at low potentials. The generation of GALD is facilitated by the Pt₆Au₄@Ag, which has a large GALD selectivity of 35% at 1.1 V. In contrast, this process is suppressed when the Pt₃Au₇@Ag and Pt₂Au₈@Ag are used, which may be due to the strong adsorption of C3 species on the Pt surface. Subsequently, DHA is dehydrated, leading to the formation of 2-hydroxypropenal/pyruvaldehyde which is further converted into LA by Cannizzaro rearrangement [41]. LA can only be detected from the Pt₃Au₇@Ag at 0.7 V. When the applied potential is increased from 0.7 to 0.9 V, FA is

produced as the consumption of LA. As a C3 product, LA can be further oxidized into FA and acetic acid, which affords one of the pathways for the formation of FA [19]. GLA is produced from oxidation of GALD. This process is clearly suppressed when the Pt₄Au₆@Ag is used. Subsequently, GLA is oxidized into GA and FA via breaking C–C bonds. This process is facilitated by the Pt₃Au₇@Ag and Pt₂Au₈@Ag at high potentials. The Pt₃Au₇@Ag and Pt₂Au₈@Ag possess abundant Au atoms, which have a dilution effect on the Pt (111) facets, leading to strong interaction with the intermediates and thus accelerating further oxidation of GLA [42,43]. The results demonstrate that these two catalysts have strong ability to break the C–C, O–H and C–H bonds, which is consistent with the results reported by Thia et al. [18]. GA can be further oxidized to GLOA via a two-electron transfer step. GLOA is not stable in alkaline solutions and can be easily oxidized to OA, which leads to negligible GLOA in this reaction system. All the catalysts produce limited OA, indicating that the generation of OA is not favorable in the reaction pathway. GA can be oxidized to FA via the cleavage of C–C bonds as indicated by the concentration profile of FA resulted from the Pt₃Au₇@Ag and Pt₂Au₈@Ag catalysts [44]. When the potential is increased from 1.1 to 1.3 V, the concentration of FA increases, which exactly compensates for the reduction of GA. A very small amount of TA is detected, which is resulted from GLA oxidation via an alternative route. TA can be further converted into OA by cleaving C–C bonds, which affords another pathway for the generation of OA [2]. For the Pt₇Au₃@Ag, Pt₆Au₄@Ag and Pt₄Au₆@Ag catalysts, no FA is obtained, which could be probably attributed to further oxidation of FA to carboxonate [45].

For the Pt_xAu_y@Ag catalysts, low applied potentials are beneficial for the formation of DHA and GALD while high potentials are favorable for the generation of GA and FA. GLA is prone to being produced at moderate potentials. In addition, the Pt_xAu_y@Ag catalysts exhibit the larger C3/C2 ratios at low potentials compared with the Pt/C and Au, which can be explained from the unique structure of the catalysts. The Pt_xAu_y@Ag NPs consist of a large amount of granular protuberances, which could provide abundant active sites for GLY molecules, thus leading to the enhancement on electrocatalytic activity and selectivity. [27,46] In addition, the Pt_xAu_y@Ag NPs consist of dominant Pt (111)



Scheme 1. Proposed reaction pathways for GLY oxidation over the catalysts in alkaline solutions.

facets in the Pt shell, which show outstanding anti-poisoning ability towards intermediates at low potentials [42]. In addition, Pt binds GLY and the intermediates strongly while the interaction of these species with Au is relatively weak. The introduction of Au atoms in Pt lattice could regulate the binding strength of adsorbates in Pt surface [47]. Meanwhile, the presence of Pt atoms could retard the oxidation of Au and facilitate the removal of the poisonous intermediates from Au surface via the formation of hydroxide species [43]. The presence of Ag atoms in the Au core would also reduce the adsorption strength of adsorbates due to the electronic effects [48]. Moreover, the strong lattice strain in the $Pt_xAu_y@Ag$ NPs can affect the bonding strength of the intermediates [31], which is also responsible for the excellent activity and selectivity.

4. Conclusion

A series of $Pt_xAu_y@Ag$ NPs with varying Pt/Au ratios were prepared via a seed-mediated growth process and further examined as electrocatalysts for GLY oxidation. The as-prepared $Pt_xAu_y@Ag$ NPs have a unique structure, consisting of Pt shell and Au/Ag core. The Pt shell is dominant with Pt (111) facets while strong lattice strain is noted from the Au/Ag core. Electrochemical results indicate that all the $Pt_xAu_y@Ag$ catalysts have higher activity in alkaline solutions than that in acidic solutions. In particular, among the catalysts, the $Pt_4Au_6@Ag$ exhibits the largest current density of 3.1 mA cm^{-2} , which is 4.7 times that of the Pt/C. HPLC results show that the $Pt_xAu_y@Ag$ catalysts tend to yield more C3 products. Among the catalysts, the $Pt_4Au_6@Ag$ possesses the largest DHA selectivity of 77.1% at 1.1 V while the $Pt_6Au_4@Ag$ exhibits the largest GALD selectivity of 35.0% at 1.1 V. The largest GLA selectivity of 34.5% is resulted from the $Pt_3Au_7@Ag$ at 0.7 V. With increasing Au content, the selectivities of C3 products decrease. When the Au content is over 60%, the selectivity of DHA decreases. The remarkable selectivity of the C3 products can be ascribed to the dominant

Pt (111) facets in the $Pt_xAu_y@Ag$ catalysts and the synergistic effects of Pt and Au/Ag atoms.

Conflict of interest

The authors declare no conflict of interest.

Acknowledgments

The project was financially supported by the National Natural Science Foundation of China (21706081) and the Shenzhen Basic Research Project (Nos. JCYJ20170307154206288 and JCYJ20170817160837382).

Appendix A. Supplementary data

Supplementary material related to this article can be found, in the online version, at doi:<https://doi.org/10.1016/j.apcatb.2019.01.009>.

References

- [1] P. Gallezot, *Chem. Soc. Rev.* 41 (2012) 1538–1558.
- [2] L.S.R. Silva, F.E. López-Suárez, M. Perez-Cadenas, S.F. Santos, L.P. da Costa, K.I.B. Eguiluz, G.R. Salazar-Banda, *Appl. Catal. B: Environ.* 198 (2016) 38–48.
- [3] C.-H. Zhou, J.N. Beltrami, Y.-X. Fan, G.Q. Lu, *Chem. Soc. Rev.* 37 (2008) 527–549.
- [4] J. Callison, N.D. Subramanian, S.M. Rogers, A. Chutia, D. Gianolio, C.R.A. Catlow, P.P. Wells, N. Dimitratos, *Appl. Catal. B: Environ.* 238 (2018) 618–628.
- [5] M. Simões, S. Baranton, C. Coutanceau, *ChemSusChem* 5 (2012) 2106–2124.
- [6] D. Hekmat, R. Bauer, J. Fricke, *Bioprocess Biosyst. Eng.* 26 (2003) 109–116.
- [7] A. Behr, J. Eilting, K. Irawadi, J. Leschinski, F. Lindner, *Green Chem.* 10 (2008) 13–30.
- [8] Y. Zhang, Z. Shen, X. Zhou, M. Zhang, F. Jin, *Green Chem.* 14 (2012) 3285–3288.
- [9] H.J. Kim, S.M. Choi, S. Green, G.A. Tompsett, S.H. Lee, G.W. Huber, W.B. Kim, *Appl. Catal. B: Environ.* 101 (2011) 366–375.
- [10] G.L. Caneppele, T.S. Almeida, C.R. Zanata, É. Teixeira-Neto, P.S. Fernández, G.A. Camara, C.A. Martins, *Appl. Catal. B: Environ.* 200 (2017) 114–120.

- [11] A.C. Garcia, M.J. Kolb, C. van Nieropy Sanchez, J. Vos, Y.Y. Birdja, Y. Kwon, G. Tremiliosi-Filho, M.T.M. Koper, *ACS Catal.* 6 (2016) 4491–4500.
- [12] Y. Kwon, K.J.P. Schouten, M.T.M. Koper, *ChemCatChem* 3 (2011) 1176–1185.
- [13] Z. Zhang, L. Xin, W. Li, *Appl. Catal. B: Environ.* 119–120 (2012) 40–48.
- [14] Y. Zhou, Y. Shen, *Electrochem. Commun.* 90 (2018) 106–110.
- [15] J. Qi, L. Xin, D.J. Chadderdon, Y. Qiu, Y. Jiang, N. Benipal, C. Liang, W. Li, *Appl. Catal. B: Environ.* 154–155 (2014) 360–368.
- [16] N. Benipal, J. Qi, Q. Liu, W. Li, *Appl. Catal. B: Environ.* 210 (2017) 121–130.
- [17] A.C. Garcia, E.B. Ferreira, V.V. Silva de Barros, J.J. Linares, G. Tremiliosi-Filho, *J. Electroanal. Chem. (Lausanne)* 793 (2017) 188–196.
- [18] L. Thia, M. Xie, D. Kim, X. Wang, *Catal. Sci. Technol.* 7 (2017) 874–881.
- [19] C. Dai, L. Sun, H. Liao, B. Khezri, R.D. Webster, A.C. Fisher, Z.C.J. Xu, *J. Catal.* 356 (2017) 14–21.
- [20] C.R. Zanata, P.S. Fernández, H.E. Troiani, A.L. Soldati, R. Landers, G.A. Camara, A.E. Carvalho, C.A. Martins, *Appl. Catal. B: Environ.* 181 (2016) 445–455.
- [21] Y. Chang, I. Lu, C. Chen, Y. Hsieh, P. Wu, *J. Alloys Compd.* 586 (2014) 507–511.
- [22] K.D. Gilroy, X. Yang, S. Xie, M. Zhao, D. Qin, Y. Xia, *Adv. Mater.* (2018) 1706312.
- [23] W. Niu, L. Zhang, G. Xu, *ACS Nano* 4 (2010) 1987–1996.
- [24] H. Chen, Z. Sun, W. Ni, K.C. Woo, H. Lin, L. Sun, C. Yan, J. Wang, *Small* 5 (2009) 2111–2119.
- [25] Y. Shen, Y. Zhou, D. Wang, X. Wu, J. Li, J. Xi, *Adv. Energy Mater.* (2017) 1701759.
- [26] Y. Shen, Y. Zhou, B. Gong, K. Xiao, L. Wang, J. Xi, *J. Catal.* 345 (2017) 70–77.
- [27] Y. Shen, Z. Zhang, K. Xiao, J. Xi, *Phys. Chem. Chem. Phys.* 16 (2014) 21609–21614.
- [28] Y. Zhou, Y. Shen, J. Piao, *ChemElectroChem* 5 (2018) 1636–1643.
- [29] Y. Sun, Y. Xia, *J. Am. Chem. Soc.* 126 (2004) 3892–3901.
- [30] S. Lai, C. Fu, Y. Chen, X. Yu, X. Lai, C. Ye, J. Hu, *J. Power Sources* 274 (2015) 604–610.
- [31] H. Wang, S. Zhou, K.D. Gilroy, Z. Cai, Y. Xia, *Nano Today* 15 (2017) 121–144.
- [32] J. Yang, J.Y. Lee, H.P. Too, *J. Phys. Chem. B* 109 (2005) 19208–19212.
- [33] W. Hong, C. Shang, J. Wang, E. Wang, *Nanoscale* 7 (2015) 9985–9989.
- [34] M. Tsuji, M. Hamasaki, A. Yajima, M. Hattori, T. Tsuji, H. Kawazumi, *Mater. Lett.* 121 (2014) 113–117.
- [35] M.A. Salem, E.A. Bakr, H.G. El-Attar, *Spectrochim. Acta A* 188 (2018) 155–163.
- [36] A.C. Garcia, Y.Y. Birdja, G. Tremiliosi-Filho, M.T.M. Koper, *J. Catal.* 346 (2017) 117–124.
- [37] S.T. Nguyen, H.M. Law, H.T. Nguyen, N. Kristian, S. Wang, S.H. Chan, X. Wang, *Appl. Catal. B: Environ.* 91 (2009) 507.
- [38] G. Li, L. Jiang, Q. Jiang, S. Wang, G. Sun, *Electrochim. Acta* 56 (2011) 7703.
- [39] A. Zalineeva, A. Serov, M. Padilla, U. Martinez, K. Artyushkova, S. Baranton, C. Coutanceau, P.B. Atanassov, *J. Am. Chem. Soc.* 136 (2014) 3937–3945.
- [40] R.K.P. Purushothaman, J.V. Haveren, D.S.V. Es, I. Melián-Cabrera, J.D. Meeldijk, H.J. Heeres, *Appl. Catal. B: Environ.* 147 (2014) 92–100.
- [41] C.H. Lam, A.J. Bloomfield, P.T. Anastas, *Green Chem.* 19 (2017) 1958–1968.
- [42] P.S. Fernández, C.A. Martins, C.A. Angelucci, J.F. Gomes, G.A. Camara, M.E. Martins, G. Tremiliosi-Filho, *ChemElectroChem* 2 (2015) 263–268.
- [43] P. Lertthahan, S. Yongprapat, A. Therdthianwong, S. Therdthianwong, *Int. J. Hydrogen Energy* 42 (2017) 9202–9209.
- [44] H. Wang, L. Thia, N. Li, X. Ge, Z. Liu, X. Wang, *ACS Catal.* 5 (2015) 3174–3180.
- [45] A. Marchionni, M. Bevilacqua, C. Bianchini, Y.X. Chen, J. Filippi, P. Fornasiero, A. Lavacchi, H. Miller, L. Wang, F. Vizza, *ChemSusChem* 6 (2013) 518–528.
- [46] N. Zhang, L. Bu, S. Guo, J. Guo, X. Huang, *Nano Lett.* 16 (2016) 5037–5043.
- [47] W. Wu, Z. Tang, K. Wang, Z. Liu, L. Li, S. Chen, *Electrochim. Acta* 260 (2018) 168–176.
- [48] A.G. Garcia, P.P. Lopes, J.F. Gomes, C. Pires, E.B. Ferreira, R.G.M. Lucena, L.H.S. Gasparotto, G. Tremiliosi-Filho, *New J. Chem.* 38 (2014) 2865–2873.